

Accurate model of liquid-liquid phase behaviour of intrinsically-disordered proteins from optimization of single-chain properties

Giulio Tesei^{a,1}, Thea K. Schulze^a, Ramon Crehuet^{a,b}, and Kresten Lindorff-Larsen^{a,1}

^aStructural Biology and NMR Laboratory & the Linderstrøm-Lang Centre for Protein Science, Department of Biology, University of Copenhagen, Copenhagen, Denmark;

^bCSIC-Institute for Advanced Chemistry of Catalonia (IQAC), Barcelona, Spain

This manuscript was compiled on September 10, 2021

1 **Many intrinsically disordered proteins (IDPs) may undergo liquid-
2 liquid phase separation (LLPS) and participate in the formation of
3 membraneless organelles in the cell, thereby contributing to the reg-
4 ulation and compartmentalisation of intracellular biochemical reac-
5 tions. The phase behaviour of IDPs is sequence-dependent, and its
6 investigation through molecular simulations requires protein mod-
7 els that combine computational efficiency with an accurate descrip-
8 tion of intra- and intermolecular interactions. We developed a gen-
9 eral coarse-grained model of IDPs, with residue-level detail, based
10 on an extensive set of experimental data on single-chain proper-
11 ties. Ensemble-averaged experimental observables are predicted
12 from molecular simulations, and a data-driven parameter-learning
13 procedure is used to identify the residue-specific model parameters
14 that minimize the discrepancy between predictions and experiments.
15 The model accurately reproduces the experimentally observed con-
16 formational propensities of a set of IDPs. Through two-body as well
17 as large-scale molecular simulations, we show that the optimization
18 of the intramolecular interactions results in improved predictions of
19 protein self-association and LLPS.**

biomolecular condensates | liquid-liquid phase separation | intrinsically disordered proteins

1 **M**any intrinsically disordered proteins (IDPs) and proteins with disordered regions can condense into liquid-like droplets, viz. a biomolecule-rich phase coexisting with a more dilute solution (1–5). This de-mixing process is known as liquid-liquid phase separation (LLPS) and is one of the ways cells compartmentalise proteins, often together with nucleic acids (6). While LLPS plays crucial biological roles in the cell, its dysregulation leads to maturation of biomolecular condensates into hydrogel-like assemblies, promoting the formation of neurotoxic oligomers and amyloid fibrils (5, 7). A quantitative model for the ‘molecular grammar’ of LLPS, including the influence of disease-associated mutations and post-translational modifications (PTMs) on the propensity to phase separate, is key to understand these processes. The sequences of IDPs and intrinsically disordered regions that easily undergo LLPS are often characterized by stretches enriched in small polar residues (spacers) interspersed by e.g. aromatic or arginine residues (stickers), which are instrumental for the formation of reversible physical cross-links via π - π , cation- π and sp^2 - π interactions (8–12). Y and R residues were shown to be necessary for the LLPS of a number of proteins including FUS, hnRNPA1, LAF-1 and Ddx4 (8, 10, 11, 13–17). While the propensity to undergo LLPS increases with the number of Y residues in the sequence, recent studies have revealed that the role of R residues is context dependent (16) and strongly affected by salt concentration (17), reflecting the unusual char-

acteristics of the R side chain (18, 19).

Here, we present the development of a coarse-grained (CG) model capable of predicting the phase behaviour of IDPs based on amino acid sequence. CG models enable the combination of a sequence-dependent description with the computational efficiency necessary to explore the long time and large length scales involved in phase transitions (11, 20, 21). Although CG molecular simulations have been employed to explain the sequence dependence of the LLPS of a number of IDPs (11, 15, 17, 20–22) as well as the effect of phosphorylation on LLPS propensities (23, 24), such models have proven difficult to use to predict the phase behaviour of very diverse sequences (25). Building on recent developments, including experimental phase diagrams of a number of IDPs (3, 4, 15, 16), we trained and tested a robust sequence-dependent model of the LLPS of IDPs. In particular, due to the similarity between intramolecular interactions within IDPs and intermolecular interactions between IDPs (12, 26), we rationalized that by optimizing a model to capture structural preferences for a broad set of monomeric IDPs, we could obtain a good model for interactions between IDPs.

The starting point for our analyses is the hydrophobicity scale (HPS) model (21) (with minor modification; see *SI Appendix*) wherein, besides steric repulsion and salt-screened charge-charge interactions, residue-residue interactions are determined by hydrophobicity parameters (λ) which were derived from the atomic partial charges of a classical all-atom force field (27). Recently, the development of the HPS-Urry model (28) presented substantial improvements in accuracy over the original HPS model. These were achieved using a hydrophobicity scale derived from transition temperatures of elastin-like peptides (29), and further shifting the λ parameters by -0.08 to improve agreement with experimentally measured radii of gyration.

To address the current limitations, we improve upon these models by optimizing the λ parameters through a Bayesian parameter-learning procedure (30–33), leveraging as prior knowledge the probability distribution of the λ parameters evaluated from analysing 87 hydrophobicity scales. The training set comprises SAXS and paramagnetic relaxation enhancement (PRE) NMR data of 45 IDPs which we selected from the literature. First, we run Langevin dynamics simulations

Author contributions: G.T., T.K.S., R.C., and K.L.-L. designed research; G.T. and T.K.S. performed research; G.T. and R.C. developed software; G.T. and T.K.S. performed molecular simulations.; G.T. and T.K.S. analyzed data; G.T. and K.L.-L. wrote the paper with input from T.K.S and R.C.

The authors declare no conflict of interest.

¹To whom correspondence should be addressed. E-mail: giulio.tesei@bio.ku.dk (G.T.) & lindorff@bio.ku.dk (K.L.-L.)

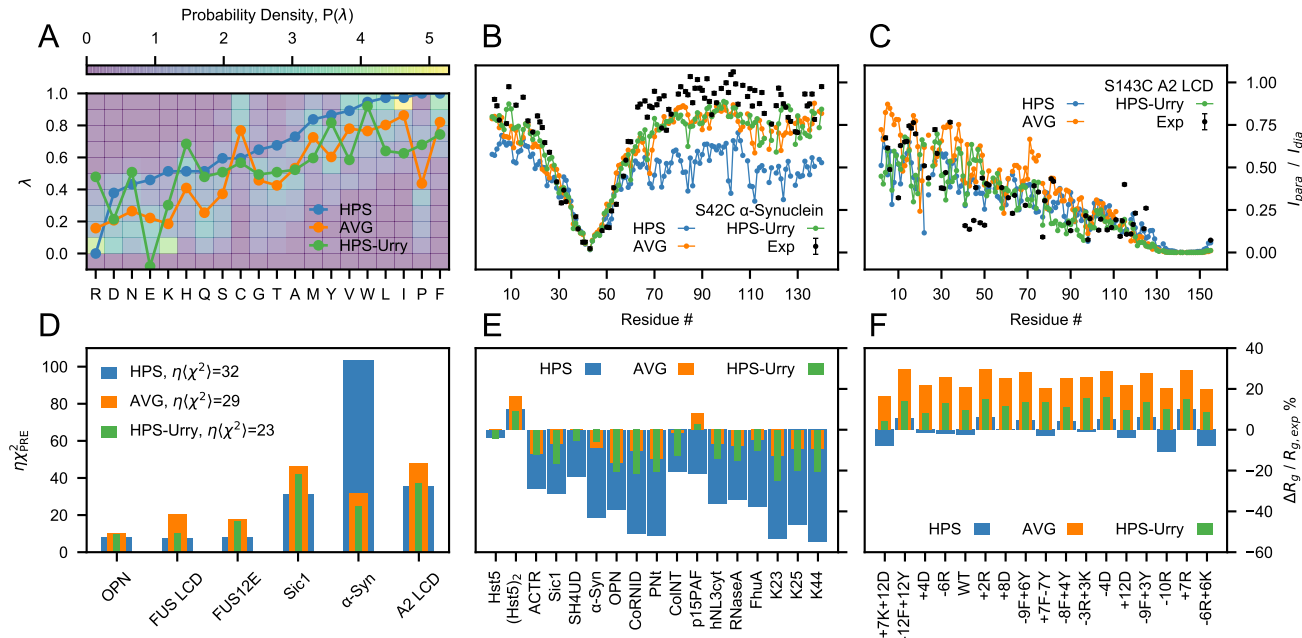


Fig. 1. Assessing the HPS, AVG and HPS-Urry models using experimental data reporting on single-chain conformational properties. (A) Probability distributions of the λ parameters calculated from 87 min-max normalized hydrophobicity scales. Lines are the λ parameters of the HPS model (blue), the average over the hydrophobicity scales (orange) and the HPS-Urry model (green) (28). Intramolecular PRE intensity ratios for the S43C mutant of α -Synuclein (B) and the S243C mutant of A2 LCD (C) from simulations and experiments (22, 37) (black). (D) χ^2 values quantifying the discrepancy between simulated and experimental intramolecular PRE data, scaled by the hyperparameter $\eta = 0.1$ (Materials and Methods). (E and F) Relative difference between simulated and experimental radii of gyration for proteins that do not readily undergo phase separation alone (E) and for variants of A1 LCD (F), with negative values corresponding to the simulated ensembles being more compact than in experiments.

of single IDPs and estimate the experimental observables using state-of-the-art methods (34). Second, we employ a Bayesian regularization approach to prevent over-fitting the training data and select three models which are equally accurate with respect to single-chain conformational properties. Third, through two-chain simulations, we validate the models by comparing predicted and experimental intermolecular PRE NMR data for the low complexity domain (LCD) of the heterogeneous nuclear ribonucleoprotein (hnRNP) A2 (A2 LCD) (22) and the LCD of the RNA-binding protein fused in sarcoma (FUS LCD) (23). Fourth, we perform coexistence simulations to test the models against the phase behaviour of A2 LCD (22, 24), FUS LCD (35, 36), variants of hnRNP A1 LCD (A1 LCD) (15, 16), the N-terminal region of the germ-granule protein Ddx4 (Ddx4 LCD) (8, 10, 13) and the N-terminal, R-/G-rich domain of the P granule protein LAF-1 (LAF-1 RGG domain). We use the final model to provide insight into the interactions between IDPs within condensates and to help elucidate the role of different amino acids to the driving force for LLPS.

Results and Discussion

Analysis of Hydrophobicity Scales. The λ values of the original HPS model are based on a hydrophobicity scale derived by Kapcha and Rossky from the atomic partial charges of the OPLS all-atom force field (27). Dozens of amino acid hydrophobicity scales have been derived from experimental as well as bioinformatics approaches such as the partitioning of amino acids between water and organic solvent, the partitioning of peptides to the lipid membrane interface and the

accessible surface area of residues in folded proteins (38, 39). To carry out the Bayesian optimisation of the amino-acid specific λ values, we sought to estimate the prior probability distribution of the hydrophobicity parameters from the analysis of 98 hydrophobicity scales collected by Simm et al. (39). Each scale was min-max normalized and, after ranking in the ascending order of the HPS scale, we discarded all the scales yielding a linear fit with negative slope. This procedure allowed us to identify scales which were present in the set both in their original form and as the additive inverse of the hydrophobicity values (reversed scales). For most scales, the selection criterion resulted in discarding the reversed form. However, for scales where the most negative values of the hydrophobicity parameter

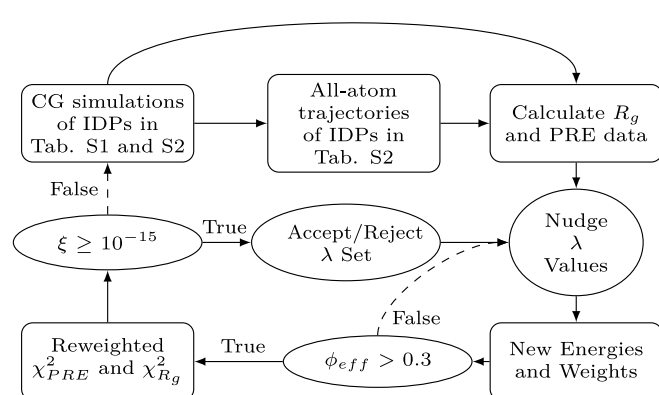


Fig. 2. Flowchart illustrating the Bayesian parameter-learning procedure (Materials and Methods).

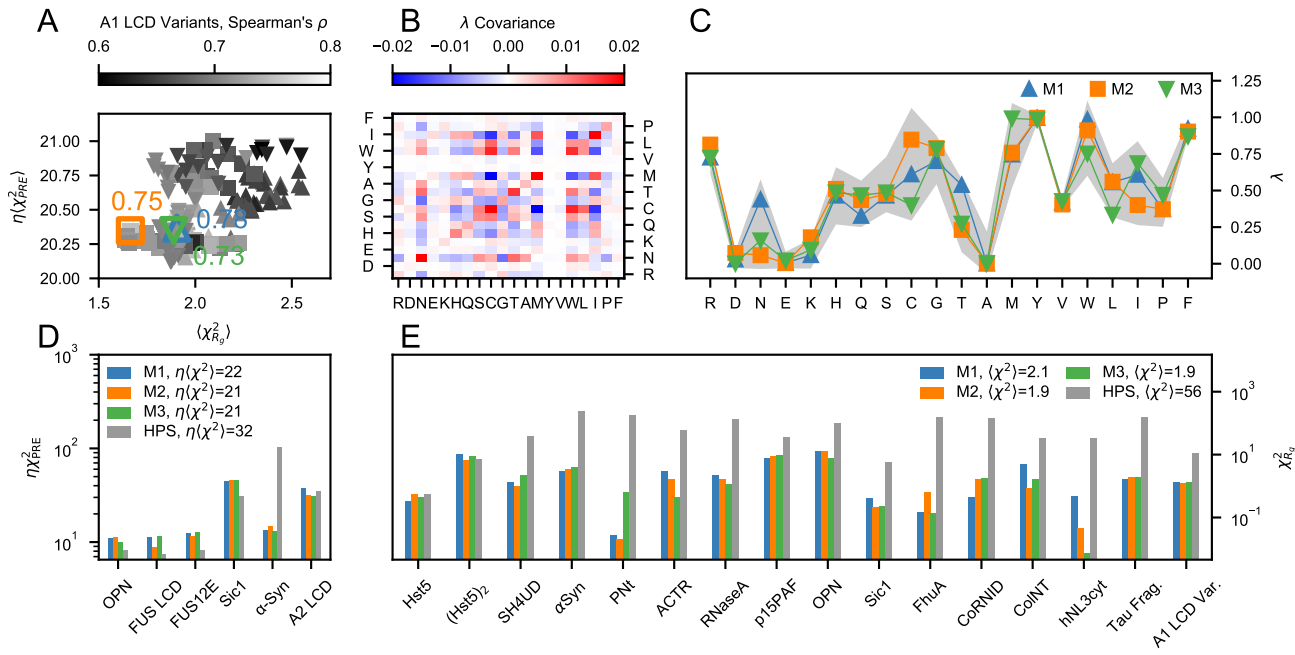


Fig. 3. Selection and performance of the M1–3 models with respect to the training data. (A) Overview of the optimal λ sets with $\eta\chi_{PRE}^2 < 21$ and $\chi_{Rg}^2 < 3$ collected through the parameter learning procedures started from $\lambda_0 = \text{AVG}$ (up triangles), M1 (squares) and M2 (down triangles). The gray gradient shows the Spearman's correlation coefficient between experimental and simulated R_g values for the A1 LCD variants in the training set. Colored open symbols indicate the M1 (blue up triangle), M2 (orange square) and M3 (green down triangle) scales whereas the adjacent values are the respective Spearman's correlation coefficients. (B) Covariance matrix of the λ sets with $\eta\chi_{PRE}^2 < 21$ and $\chi_{Rg}^2 < 3$. (C) M1 (blue), M2 (orange) and M3 (green) scales. Solid lines are guides for the eye whereas the gray shaded area shows the mean $\pm 2\text{SD}$ of the λ sets with $\eta\chi_{PRE}^2 < 21$ and $\chi_{Rg}^2 < 3$. (D–E) Comparison between (D) $\eta\chi_{PRE}^2$ and (E) χ_{Rg}^2 values for the HPS model (gray) and the optimized M1 (blue), M2 (orange) and M3 (green) models.

111 correspond to the most hydrophobic amino acids—such as the
 112 scales by Bull and Breese (40), Guy (41), Bishop et al. (42)
 113 and Welling et al. (43)—we retained only the reversed form.
 114 The 87 scales that remained after this filtering were used to
 115 calculate the average scale (AVG) and the probability distribution
 116 of the λ values for the 20 amino acids, $P(\lambda)$, which is
 117 normalized so that $\sum_{aa} \int_{\lambda_{aa}=0}^{\lambda_{aa}} P(\lambda_{aa}) d\lambda_{aa} = 20$ (Fig. 1A).
 118 For the optimization described below we use the AVG scale as
 119 starting point, as well as an indication of the typical accuracy
 120 obtained from the prior knowledge encoded in $P(\lambda)$.

121 We assessed the HPS, HPS-Urry and AVG parameter sets
 122 by running simulations of 45 IDPs ranging in length between
 123 24 and 334 residues and compared the results against experiments.
 124 Specifically, we compared the simulations with the radii of gyration, R_g , of 42 IDPs (Tab. S1) and intramolecular
 125 PRE data of six IDPs (Tab. S2) (16, 22, 23, 37, 44–57). Com-
 126 pared to the AVG scale, the HPS model overestimates the
 127 compaction of α -Synuclein whereas it closely reproduces the
 128 PRE data for A2 LCD (Fig. 1B and C). In general, the HPS
 129 model accurately predicts the conformational properties of
 130 sequences with high LLPS propensity, e.g. FUS LCD, A2 LCD
 131 and A1 LCD (Fig. 1D and F), while the AVG scale is consid-
 132 erably more accurate at reproducing the R_g of proteins that
 133 do not readily undergo phase separation alone (Fig. 1E). The
 134 recently proposed HPS-Urry model (28) is the most accurate
 135 at predicting the intramolecular PRE data while it shows inter-
 136 mediate accuracy for the R_g values of both proteins that do
 137 not readily undergo phase separation alone and A1 LCD vari-
 138 ants. The HPS-Urry model in particular differs significantly
 139 from the HPS and AVG models for the λ parameters for R

140 and E as well as the reversal of the order of hydrophobicity of
 141 Y and F (Fig. 1A).

Optimization of Amino-Acid Specific Hydrophobicity Values.

142 To obtain a model that more accurately predicts the confor-
 143 mational properties of IDPs of diverse sequences and LLPS
 144 propensities, we trained the λ values on a large set of experi-
 145 mental R_g and PRE data using a Bayesian parameter-learning
 146 procedure (30) shown schematically in Fig. 2 (Materials and
 147 Methods). We initially performed an optimization run starting
 148 from the AVG λ values and setting the hyperparameters to
 149 $\theta = \eta = 0.1$ (Fig. S1A). We collected the optimized sets of
 150 λ values which yielded $\eta\chi_{PRE}^2 < 21$ and $\chi_{Rg}^2 < 3$ (circles in
 151 Fig. 3A). The optimization was repeated starting from all
 152 $\lambda = 0.5$ to assess that the parameter space sampled by our
 153 method is independent of the initial conditions (Fig. S2A and
 154 S1D). Thus, while we used the AVG model as starting point,
 155 our final parameters only depend on $P(\lambda)$ via its use as the
 156 prior in the Bayesian optimization.

157 From the pool of optimized parameters, we selected the
 158 λ set which resulted in the largest Spearman's correlation
 159 coefficient ($\rho = 0.78$) between simulated and experimental R_g
 160 values for the A1 LCD variants. We base this final selection
 161 of the optimal λ set on the Spearman's correlation coefficient
 162 of the A1 LCD variants because we expect that capturing
 163 the experimental ranking in chain compaction will result in
 164 accurate predictions of the relative LLPS propensities (15,
 165 16, 20, 58, 59). Further, the systematic mutagenesis studies
 166 enable us to more clearly decouple the parameters for Y-vs-F
 167 and R-vs-K (15, 16). We note that while this selection uses
 168

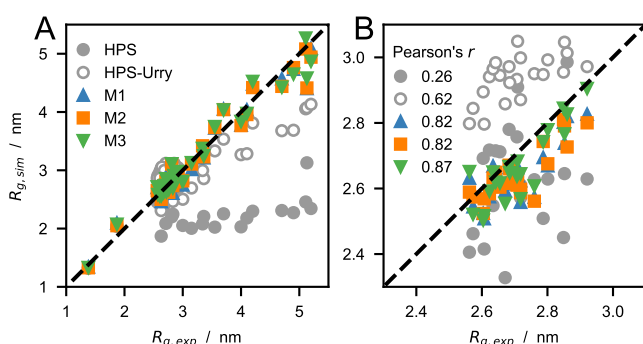


Fig. 4. (A) Comparison between experimental and predicted radii of gyration (Tab. S1), R_g , for the HPS, HPS-Urry, and M1–3 models. (B) Zoom-in on the R_g values of the A1 LCD variants, with Pearson's r coefficients for this subset of the training data reported in the legend.

only the A1 LCD variants, all three parameter sets result in good agreement with the full PRE and R_g data set (Fig. 3A).

The selected model, referred to as M1 hereafter, is the starting point for two consecutive optimization cycles (Fig. S1B) which were performed with a lower weight for the prior ($\theta = 0.05$), yielding a new pool of optimized parameters (squares in Fig. 3A) and model M2 (largest $\rho = 0.75$). To generate a third model, we further decreased the confidence parameter to $\theta = 0.02$ and performed an additional optimization run starting from M2 (Fig. S1C). From the collected optimal parameters (triangles in Fig. 3A), we selected M3 (largest $\rho = 0.73$). As shown in Fig. 3B, the optimal λ values collected through the four independent optimization runs (Fig. S1A–D) are weakly intercorrelated. The covariance values range between -0.015 and 0.015 for most amino acids, with the exception of the standard deviations of N, C, T, M, W, and I. C, M, W, and I are among the least frequent amino acids in the training set (Fig. S3) and, unsurprisingly, we observe the largest covariance values for C-W (0.017), C-M (-0.02) and C-I (-0.016). Fig. 3C shows that M1–3 fall within two standard deviations (SDs) above and below the mean of the λ values yielding $\eta\chi_{PRE}^2 < 21$ and $\chi_{R_g}^2 < 3$ (gray shaded area). Despite their differences, M1–3 fit the training data equally accurately and result in an improvement in χ_{PRE}^2 and $\chi_{R_g}^2$ of ~30% and ~95% with respect to the HPS model, respectively (Fig. 3D and E).

Notably, the optimization procedure captures the sequence dependence of the chain dimensions (Fig. 4) and results in accurate predictions of intramolecular PRE data for both highly soluble IDPs and proteins that more readily phase separate (Fig. S4B–D and Fig. S5–S10), as well as in radii of gyration with relative errors $-14\% < \Delta R_g / R_{g,exp} < 12\%$ (Fig. S4E and F). Besides reproducing the experimental R_g values for the longer chains with high accuracy, the optimized models also capture the differences in R_g and scaling exponents, ν , for the variants of A1 LCD (Fig. 4B and S11). The lower Pearson's correlation coefficients observed for ν , compared to the corresponding R_g data, may originate from the different models used to infer ν from SAXS experiments and simulation data, i.e., respectively, the molecular form factor method (16, 52) and least-squares fit to long intramolecular pairwise distances, R_{ij} , vs $|i - j| > 10$ (60) (Fig. S12).

To assess the impact of phase separating proteins on the optimized models, we perform an optimization run wherein the

A1 LCD variants are removed from the training set. The major difference between the resulting optimal λ set and models M1–3 is the considerably smaller values for R and Y residues (Fig. S2C). Indeed, the large λ values for R and Y residues in M1–3 relative to the HPS, AVG and HPS-Urry models, is a striking feature which resonates with previous experimental findings pointing to the important role of R and Y residues in driving LLPS (8, 14–16, 22, 61, 62).

To identify the hydrophobicity scales which most closely resemble M1–3, we construct a dendrogram (Fig. S13) complementing the 87 scales retained from the set by Simm et al. (39) with the Urry, Kapcha-Rosky and M1–3 scales, and using average linkage-based hierarchical clustering and Euclidean distances as the metric. This analysis reveals that the hydrophobicity scales by Urry et al. (29), Bishop et al. (42), Wimley and White (63) and the membrane protein surrounding hydrophobicity scale by Ponnuswamy and Gromiha (64) are those with greatest similarity to M1–3. These scales, which are characterized by a λ value for the R residue above the 80% quantile, are possibly the best of the unmodified scales for the properties that we optimized M1–3 to reproduce.

Testing Protein-Protein Interactions. To test whether the parameters trained on single-chain conformational properties are transferable to protein-protein interactions, we compared experimental intermolecular PRE rates, Γ_2 , of FUS LCD and A2 LCD (22, 23) with predictions from two-chain simulations of the M1–3 models performed at the same conditions as the reference experiments. Intermolecular Γ_2 values were obtained from solutions of spin-labeled ^{14}N protein and ^{15}N protein without a spin-label in equimolar amount and report on the transient interactions between a paramagnetic nitroxide probe attached to a cysteine residue of the spin-labeled chain and all the amide protons of the ^{15}N -labeled chain. We carried out the calculation of the PRE rates using DEER-PREDict (34), assuming an effective correlation time of the spin label, τ_t , of 100 ps and fitting an overall molecular correlation time, τ_c , within the interval $1 \leq \tau_c \leq 20$ ns. In agreement with experiments, Γ_2 values predicted by the M1–3 models are characterized by no distinctive peaks along the protein sequence (Fig. 5A–E), which is consistent with transient and non-specific protein–protein interactions. Notably, while PRE rates for FUS LCD are of the same magnitude for all spin-labeled sites, the A2 LCD presents larger Γ_2 values for S99C than for S143C indicating that the tyrosine-rich aggregation-prone region (residues 84–107) is involved in more frequent intermolecular contacts with the entire sequence. The discrepancy between predicted and experimental intermolecular PRE data, χ_{PRE}^2 , varies significantly as a function of τ_c (Fig. 5F–G). For both FUS LCD and A2 LCD, the optimal τ_c is larger for M1 than for M3, which suggests that the latter has more attractive intermolecular interactions. While for M1 the minimum of χ_{PRE}^2 is at $\tau_c = 17$ ns for both proteins, for M3 the optimal τ_c value is ~8 ns smaller for FUS LCD than A2 LCD. Although the accuracy of τ_c is difficult to assess in the case of transiently interacting IDPs, this large difference in τ_c (Fig. 5) suggests that the protein-protein interactions predicted for FUS LCD by M3 may be overly attractive.

To quantify protein-protein interactions with the optimized models, we calculated second virial coefficients, B_{22} , from two-chain simulations (*SI Appendix*). The net interactions are attractive for both the sequences ($B_{22} < 0$), and considerably

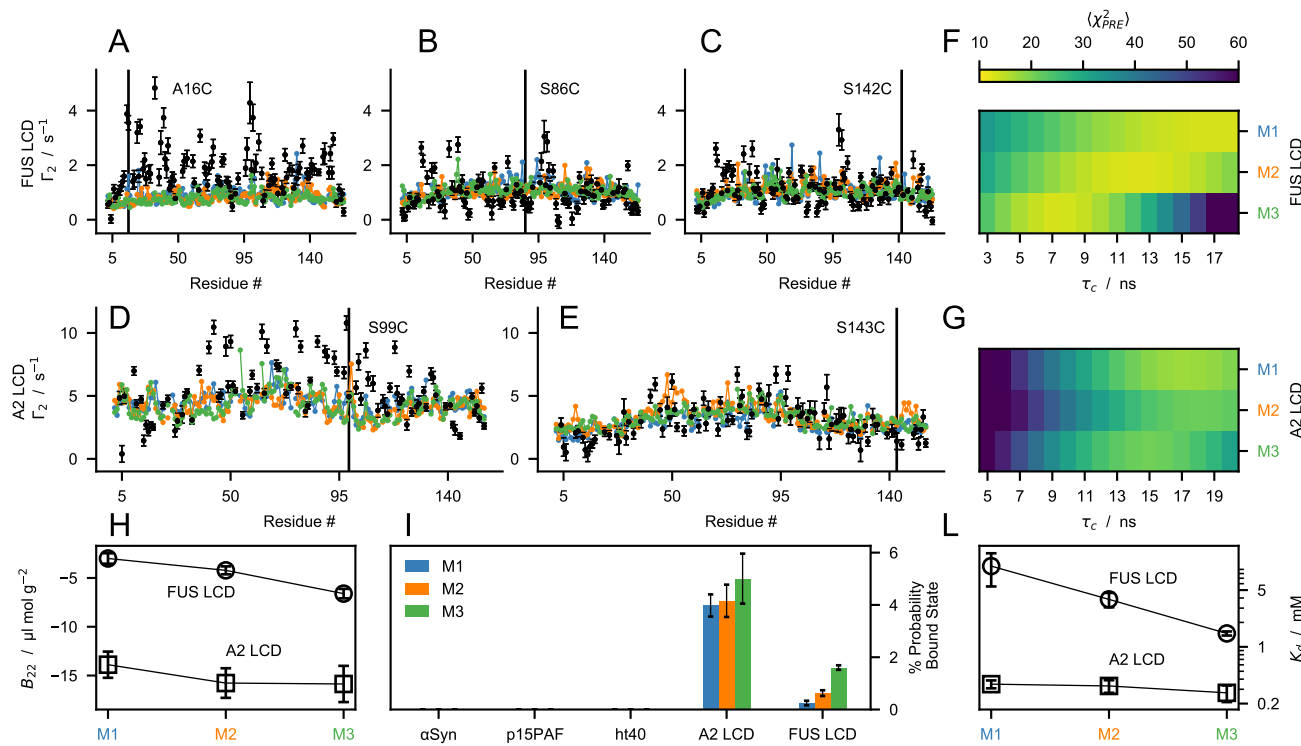


Fig. 5. Testing the M1–3 models using experimental findings on protein–protein interactions. (A–E) Comparison between experimental (black) intermolecular PRE rates (Tab. S3) and predictions from the M1 (blue), M2 (orange) and M3 (green) models for FUS LCD (A–C) and A2 LCD (D–E) calculated using the best-fit correlation time, τ_c . (F–G) Discrepancy between calculated and experimental intermolecular PRE rates χ^2_{PRE} as a function of τ_c . (H) Second virial coefficients, B_{22} , of FUS LCD (circles) and A2 LCD (squares) calculated from two-chain simulations of the M1–3 models. Error bars are SEMs estimated by bootstrapping 1,000 times 40 B_{22} values calculated from trajectory blocks of 875 ns. (I) Probability of the bound state estimated from protein–protein interaction energies in two-chain simulations of the M1–3 models. (L) Dissociation constants, K_d , of FUS LCD (circles) and A2 LCD (squares) calculated from two-chain simulations of the M1–3 models. For p_B and K_d , error bars are SDs of ten simulation replicas. Lines in H and L are guides to the eye.

stronger for A2 LCD than for FUS LCD. As expected from the λ values and amino acid compositions, M3 presents the most negative B_{22} values (large λ values for Q, G and P), followed by M2 and M1 (Fig. 5I).

To test whether predictions of protein self-association by M1–3 are sequence dependent, we compared the probability of finding proteins in the bound dimeric state, p_B , in simulations of α -Synuclein, p15PAF, full length tau (ht40), A2 LCD and FUS LCD performed at the solution conditions of the reference experimental data (37, 50, 65) (SI Appendix). In agreement with experimental findings, we find that the highly soluble α -Synuclein, p15PAF and ht40 proteins do not self-associate substantially in our simulations, whereas A2 LCD and FUS LCD have $p_B \sim 4\%$ and $\sim 1\%$, respectively. We further estimated the dissociation constants of A2 LCD and FUS LCD using $K_d = (1-p_B)^2/(N_A p_B V)$ and $K_d = 1/(N_A p_B (V - B_{22}))$ self-consistently (66), where N_A is Avogadro's number (SI Appendix, Fig. 5L and S14).

Testing LLPS propensities. To test the ability of the models to capture the sequence-dependence of LLPS propensity, we performed multi-chain simulations in a slab geometry and calculated protein concentrations of the coexisting condensate, c_{con} , and dilute phase, c_{sat} . We compared our simulation results to an extensive set of sequences which have been shown to undergo LLPS below an upper critical solution temperature (UCST), namely FUS LCD (23, 35, 36), A2 LCD (22, 24), the

NtoS variant of A2 LCD (24), LAF-1 RGG domain (11, 67–69), as well as variants of A1 LCD (15, 16) and Ddx4 LCD (8, 10, 13). From simulations of the optimized models at 37°C, we observed that, for a number of sequences in the test set, the predicted c_{sat} values are too low to allow for converged estimates from μ -timescale trajectories (Fig. S15). Conversely, the least LLPS-prone variants of Ddx4 LCD yielded one-phase systems when simulated at 37°C using HPS-Urry and M1–3 models. Thus, to be able to estimate converged c_{sat} values (Fig. S16, S17 and S18), simulations were carried out at 50°C, except for the HPS-Urry model which we simulated at 24°C (Tab. S4). The FtoA and RtoA variants of Ddx4 LCD were also simulated at 24°C using the M1–3 models as in simulations of the same systems at 50°C we only observed a single phase.

Simulations using M1 at 50°C most closely recapitulate the experimental trend in c_{sat} across the diverse sequences (Fig. 6A, D and G) and reproduce the reference c_{con} and c_{sat} values measured at room temperature. Conversely, HPS overestimates the relative LLPS propensity of FUS LCD, whereas simulations using HPS-Urry at 24°C show deviations of about an order of magnitude from the reference c_{sat} values for A2 LCD, Ddx4 LCD, A1 LCD and FUS LCD. Regarding the LAF-1 RGG domain, all of the models overestimate by at least a factor of ~ 5 the experimental c_{con} (68, 69), whereas M1 reproduces within a factor of ~ 2 the experimental c_{sat} value from temperature-dependent turbidity measurements (11), both for the WT and for variants with randomly shuffled

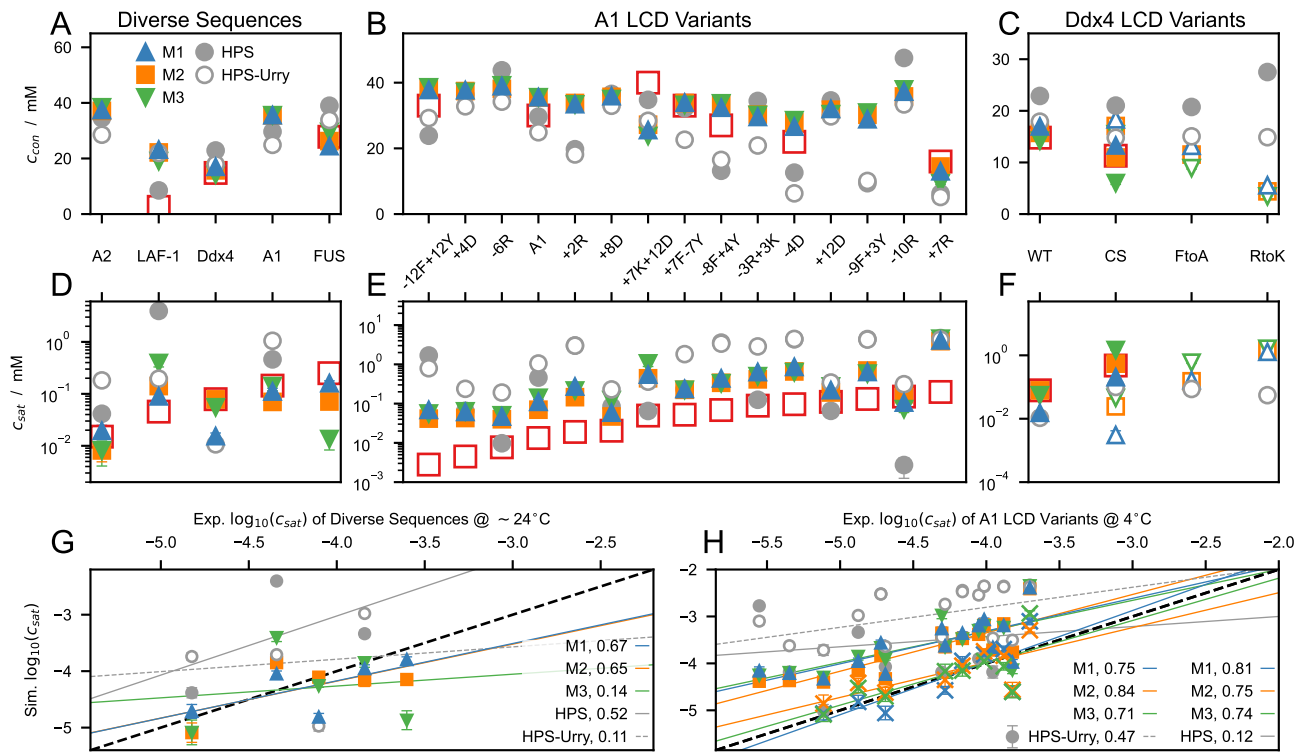


Fig. 6. Protein concentrations in the condensate (A–C) and in the dilute phase (D–F) from slab simulations of the M1–3, HPS and HPS-Urry models performed at 50°C (closed symbols), 37°C (crosses in (H)) and 24°C (open symbols). Red open squares show experimental measurements at ~24°C (A, D, C and F) and ~4°C (B and E). (G and H) Correlation between $\log_{10}(c_{sat}/M)$ from simulations and experiments for diverse sequences (G) and A1 LCD variants (H). Solid lines show linear fits to the simulation data at 50°C. Dashed lines show linear fits to the HPS-Urry data at 24°C (G and H) and to the M1–3 data at 37°C (H). Values reported in the legends are Pearson’s correlation coefficients. Error bars are SEMs of averages over blocks of 0.3 μ s. We note that the correlation coefficients reported in G are associated with a substantial uncertainty as they are calculated over only three (HPS), four (HPS-Urry) and five points (M1–3).

sequence (LAF-1 shuf) and without residues 21–30 (LAF-1 Δ 21–30) (Fig. S19). Although M1–3 fit the training data equally well, the prediction of LLPS propensities for the diverse sequences in Fig. 6A and D differ considerably, with Pearson’s correlation coefficients between simulation and experimental $\log_{10}(c_{sat})$ values ranging from 0.67 for M1 to 0.14 for M3 (Fig. 6G). The discrepancy is particularly evident for the Ddx4 LCD and FUS LCD which are rich in N and Q residues, respectively, i.e., the residues for which the M1 and M3 λ sets differ the most.

We further test our predictions against 15 variants of A1 LCD (Fig. 6B and E). These include aromatic and charge variants, which were designed to decipher the role on the driving forces for phase separation of Y vs F residues and of R, D, E and K residues, respectively (16). The nomenclature, $\pm N_X X \pm N_Z Z$, denotes increase or decrease in the number of residues of type X and Z with respect to the WT, which is achieved by mutations to or from G and S residues while maintaining a constant G/S ratio. M1–3 are found to be equally accurate, and present a considerable improvement over previous models with respect to their ability to recapitulate the trends in LLPS propensity for the aromatic and charged variants of A1 LCD. Since M1–3 were selected based on their performance in predicting the experimental ranking for the R_g values of 21 A1 LCD variants (Tab. S1), this result supports our model development strategy. For M1–3, Pearson’s correlation coefficients exceed 0.7 between $\log_{10}(c_{sat})$ values measured at 4°C (16) and simulation predictions at both 50°C and 37°C

(Fig. 6H). Moreover, c_{sat} values from simulations at 37°C are in agreement with the reference c_{sat} values at 4°C (Fig. 6H and S15). As we observed for the diverse sequences, quantitative agreement with the experimental c_{sat} values is achieved by carrying out simulations of the M1 model at a temperature systematically larger by ~30°C than the experimental conditions. In addition to the lack of temperature dependence of the hydrophobicity parameters (70), the inconsistency between the temperature dependence of chain compaction and phase separation might be attributed to more general aspects of the model. For instance, the significant decrease in the number of interaction sites upon coarse-graining at the amino-acid level, and the resulting reduction in configurational entropy (71, 72), which may promote LLPS by lowering the entropic penalty associated with partitioning a chain from the dilute solution to the condensate.

M1–3 reproduce the experimental ranking for LLPS propensity of the Ddx4 LCD variants, i.e. WT \gg CS $>$ FtoA \gtrsim RtoK (Fig. 6C and F) and, for all the variants, M1 and M3 consistently display the highest and lowest LLPS propensities, respectively. Simulations at 50°C using M2 are in quantitative agreement with the experimental c_{sat} values (13) for both WT and the CS variant, which has the same net charge and amino acid composition as the WT but a more uniform charge distribution along the sequence. Moreover, as observed experimentally (13), M1–3 predict a single phase for the RtoK variant at 24°C. As previously shown by Das et al. (25), the HPS model predicts a considerable increase in LLPS propensity

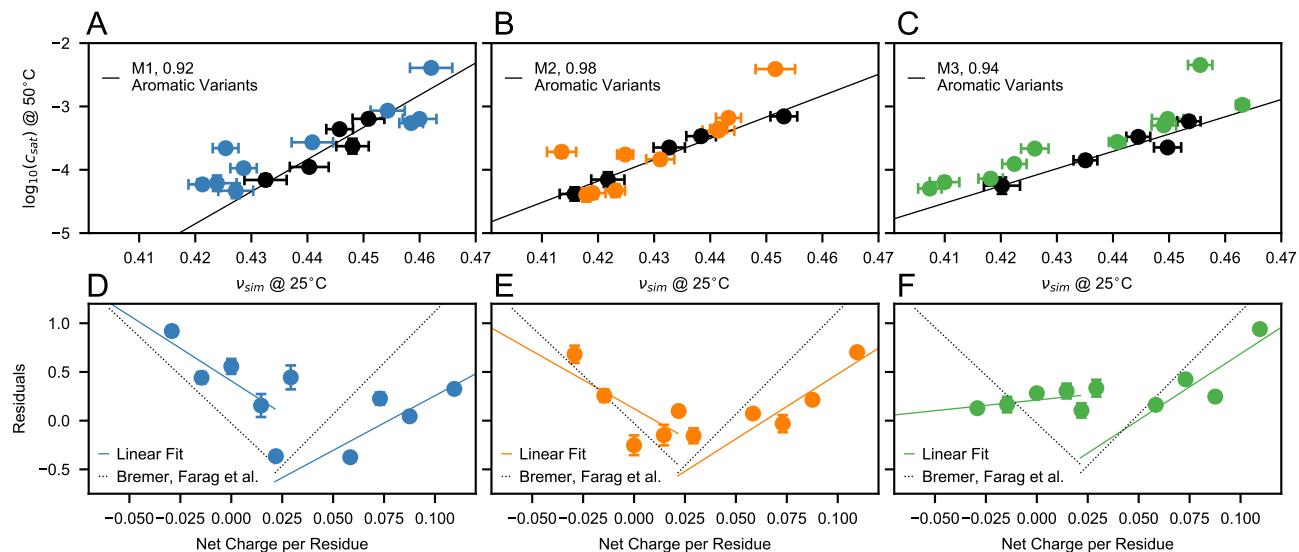


Fig. 7. Correlation between chain compaction and LLPS propensity for aromatic and charge variants of A1 LCD. (A–C) $\log_{10}(c_{sat})$ vs v_{sim} for A1 LCD variants from simulations performed using the M1 (A), M2 (B) and M3 (C) models. Black and colored circles indicate aromatic and charge variants, respectively. Black lines are linear fits to the aromatic variants. (D–F) Residuals from the linear fits of panels A–C for the charge variants of A1 LCD as a function of the net charge per residue. Values reported in the legends are Pearson's correlation coefficients. Error bars of $\log_{10}(c_{sat})$ values are SEMs of averages over blocks of 0.3 μs . Error bars of v_{sim} are SDs from fits to $R_{ij} = R_0 |i - j|^{v_{sim}}$ in the long-distance region, $|i - j| > 10$. Solid lines are linear fits to the data. Dotted lines in D–F are lines of best fit to the experimental data by Bremer, Farag et al. (16).

upon replacement of all 24 R residues in the Ddx4 LCD with K (RtoK variant; Fig. 6C), in apparent contrast to experimental observations (10, 13). Interestingly, augmenting the HPS model with stronger cation- π interactions for R-aromatic than for K-aromatic pairs (25) has been shown to be insufficient to capture the lower LLPS propensity of the RtoK variant compared to WT. On the other hand, our data for the M1–3 and HPS-Urry models indicates that making all the interactions involving R more favourable results in more accurate predictions. In fact, a large λ value for R may better mimic its relatively unfavorable free energy of hydration (19) as well as the occurrence of R-aromatic cation- π interactions, R-R π -stacking and R-D/E bidentate H-bonding (10, 17, 18, 73). Compared to the Kapcha-Rosssky scale, it is noteworthy that the increase in the λ values of R, Y and G in M1–3 is accompanied by an overall decrease in the average λ value. Hence, the optimization procedure led to the enhancement of specific attractive forces while maintaining a balance between electrostatic and non-electrostatic interactions (25), which reveals itself, for example, in the ability of M1–3 to recapitulate the lower LLPS propensity of the CS variant with respect to Ddx4 LCD WT.

The M1 and M2 parameter sets differ mainly for the λ value of the N residue (Fig. 3C) and perform equally well against the test set (Fig. 6). Therefore, we further test the ability of M1 and M2 to predict the LLPS propensity of the NtoS variant of A2 LCD with respect to the wild type. Only the M1 model, which has λ values for N and S of similar magnitude correctly predicts approximately the same LLPS propensity for variant and WT (Fig. S20), in agreement with experiments (24).

415 Correlating single-chain properties and phase separation. 416 Motivated by recent experiments on the A1 LCD (15, 16),

417 we perform a detailed analysis of the coupling between chain
418 compaction and phase behaviour of the A1 LCD variants. In
419 agreement with previous observations (16), the $\log_{10}(c_{sat})$ values
420 for the aromatic variants show a linear relationship with
421 the scaling exponent, v_{sim} , whereas changes in the number of
422 charged residues (charge variants) result in significant devi-
423 tions from the lines of best fit (Fig. 7A–C). Following the
424 approach of Bremer, Farag et al. (16), we plot the residuals
425 for the charge variants with respect to the lines of best fit as
426 a function of the net charge per residue (NCPR) (Fig. 7D–F).
427 The results for M1 and M2 show the V-shaped profile observed
428 for the experimental data (16), and support the suggestion
429 that mean-field electrostatic repulsion between the net charge
430 of the proteins is responsible for breaking the coupling between
431 chain compaction and LLPS propensity (16). In agreement
432 with experimental data (16), we observe that for M1 and M2
433 the driving forces for LLPS are maximal for small positive
434 values of NCPR (~ 0.02).

435 The dependence of LLPS on NCPR is clarified by comparing
436 the residual non-electrostatic energy maps of +8D (NCPR=0),
437 +4D (NCPR ≈ 0.03) and -4D (NCPR ≈ 0.09) with respect to the
438 wild type of A1 LCD (NCPR ≈ 0.06) (Fig. S21 and S22). While
439 in the case of NCPR=0 the residual interaction patterns within
440 the isolated chain and between chains in the condensate largely
441 overlap, the energy baselines are clearly down- and up-shifted
442 for NCPR ≈ 0.03 and NCPR ≈ 0.09 , respectively (Fig. S21G–I
443 and S22G–I). Although the interaction patterns are still dom-
444 inated by the stickers, deviations of the NCPR from ~ 0.02
445 result in electrostatic mean-field repulsive interactions that
446 disfavor LLPS. The LLPS-promoting effect of small positive
447 NCPR values finds explanation in the amphiphilic character
448 of the R side chains (18) which compensate for the repulsion
449 introduced by the excess positive charge by allowing for favor-
450 able interactions with both Y and negatively charged residues.

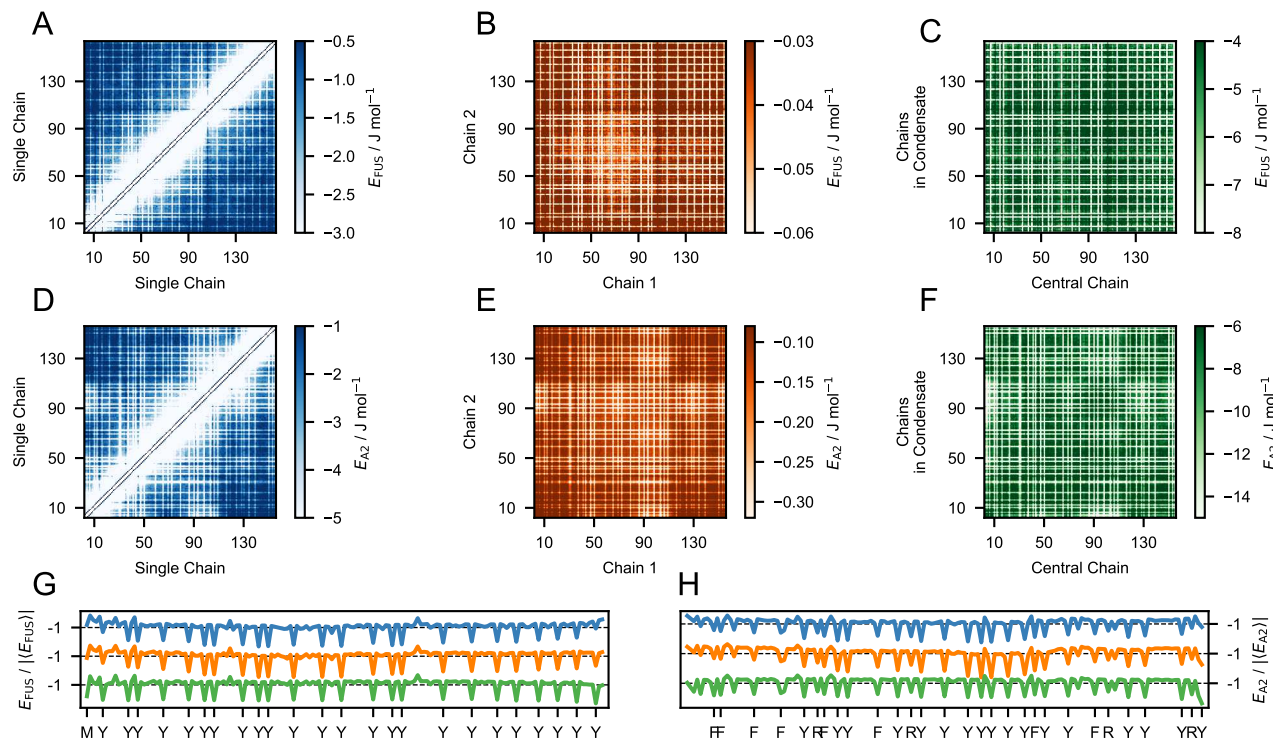


Fig. 8. Comparing residue-residue interactions in dilute solution and in the condensate. Energy maps from simulations of the M1 model of FUS LCD (A–C) and A2 LCD (D–F) calculated using non-electrostatic interaction energies. (G–H) 1D projections of the energy maps for FUS LCD (G) and A2 LCD (H), normalized by the absolute average interaction energy $|\langle E \rangle|$ and shifted vertically for clarity. Colors indicate that the energies were calculated within a single chain at infinite dilution (blue), between two chains in the dilute regime (orange) and between a chain located at the center of a condensate and the surrounding chains (green).

451 As opposed to M1–2, the readily phase-separating M3 model
 452 shows a weaker dependence on NCPR, especially for variants
 453 of net negative charge. This suggests that the experimental
 454 observations regarding the coupling between conformational
 455 and phase behaviour of A1 LCD stem from a well-defined
 456 balance between mean-field repulsion and sticker-driven LLPS
 457 which can be offset by an overall moderate increase of 3–4%
 458 in the λ values of the residues present in A1 LCD.

459 **Comparing intra- and inter-molecular interactions.** After es-
 460 tablishing the ability of model M1 to accurately predict trends
 461 in LLPS propensity for diverse sequences, we analyze the non-
 462 electrostatic residue-residue energies for FUS LCD and A2
 463 LCD within a single chain, as well as between pairs of chains in
 464 the dilute regime and in condensates. We find a striking simi-
 465 larity between intra- and intermolecular interaction patterns
 466 for both proteins (Fig. 8), consistent with a mostly uniform
 467 distribution of stickers along the linear sequence (Fig. 8G
 468 and H) (15, 74). Notably, besides the aromatic F and Y
 469 residues, the analysis also identifies an M residue and four R
 470 residues as stickers in FUS LCD and A2 LCD, respectively.
 471 Therefore, the parameter-learning procedure presented herein
 472 corroborates the important role of R as a sequence depen-
 473 dent sticker (16), whereby the large λ value for R in models
 474 M1–3 presumably reflects the ability of the amphiphilic guani-
 475 dinium moiety to engage in H-bonding, as well as π stacking
 476 and charge- π interactions (18). Further, in the dilute regime,
 477 the intra- and intermolecular interactions are weaker in the
 478 N- and C-terminal regions than for the rest of the chain, as

479 evident from the upturning baselines of the 1D interaction
 480 energy projections. This result is consistent with the faster
 481 local motions of the terminal residues inferred from ^{15}N NMR
 482 relaxation data for both unfolded proteins (75) and a number
 483 of phase separating IDPs (15, 22, 23). We also find that the
 484 aggregation-prone Y-rich region of A2 LCD (residues 84–107)
 485 interacts with the entire polypeptide chain (Fig. 8D–F) and
 486 thus likely drives chain compaction, self-association as well as
 487 LLPS. Finally, in line with previous observations from theory,
 488 simulations and experiments (16, 76, 77), we observe that the
 489 polypeptide chains of A1 LCD, A2 LCD and FUS LCD are
 490 more expanded in the condensed phase than in the dilute
 491 phase (Fig. S23). In particular, we find that the scaling expo-
 492 nents of the LCDs increase towards $\nu = 0.5$ in the condensed
 493 phase, and that differences in compaction between wild-type
 494 and charge variants of A1 LCD are greater in the dilute than
 495 in the condensed phase (Fig. S23).

496 Conclusions

497 In this work we implement and validate an automated pro-
 498 cedure to develop an accurate model of the LLPS of IDPs based
 499 on experimental data reporting on single-chain conformational
 500 properties. We show that this strategy succeeds, in agreement
 501 with the previously observed coupling between chain com-
 502 paction and propensity for phase separation (15, 20, 58, 59),
 503 but also appears to recapitulate the recent discovery that
 504 charge effects may break this relationship (16). Our work
 505 differs from related previous studies (28, 30, 33, 78) in several
 506 ways including the size of the data set used for optimization,

507 the use of both NMR PREs and R_g values, and the introduction
 508 of a prior for the λ values. Moreover, by carrying out
 509 model optimizations with and without the A1 LCD variants,
 510 we show that the presence of phase-separating IDPs in the
 511 training set helps the parameter-learning procedure to capture
 512 the role of Y and R residues as stickers. The accuracy and
 513 general applicability of our model can be tested further by
 514 future experiments on systems that were not used for training
 515 or testing. We also note that our automated, Bayesian
 516 optimization approach makes it relatively straightforward to
 517 continue to develop and improve the model as additional data
 518 becomes available.

519 Simulations performed using the model optimized herein
 520 reveal that, at least for sequences characterized by a relatively
 521 uniform distribution of stickers, residue-residue interactions
 522 determining chain compaction also drive self-association and
 523 LLPS. Moreover, we show that the experimentally-observed
 524 dependency of LLPS on protein net charge appears to be
 525 captured by salt-screened electrostatic repulsion, even when
 526 assuming a uniform dielectric constant throughout the two-
 527 phase system.

528 We have here shown how our model may be used to help
 529 elucidate the residues that are important for LLPS of IDPs
 530 with UCST behaviour. Further, we suggest the model could be
 531 applied to study the influence of disease-associated mutations
 532 on the material properties of protein self-coacervates (79, 80),
 533 the LLPS of protein mixtures as a function of composition, and
 534 the partitioning of proteins that do not readily undergo phase
 535 separation alone into condensates formed by other proteins
 536 (81, 82). Finally, owing to the generalized parameter-learning
 537 approach, the model could readily be refined as new experi-
 538 mental data are collected and it should be possible to extend
 539 it to account for specific pairwise interactions such as cation- π
 540 interactions (25), PTMs (83), the salting-out effect (84) and
 541 the temperature dependence of solvent mediated interactions
 542 (70).

543 Materials and Methods

544 We use the Ca -based model proposed by Dignon et al. (21) aug-
 545 mented with extra charges for the termini and a temperature-
 546 dependent treatment for dielectric constant of water (SI Appendix).
 547 Langevin dynamics simulations are conducted using HOOMD-blue
 548 v2.9 (85) in the *NVT* ensemble using the Langevin thermostat with
 549 a time step of 5 fs and friction coefficient 0.01 ps⁻¹ (SI Appendix).
 550 Additionally, 100- and 300-chain simulations of LAF-1 RGG domain
 551 are also performed using openMM v7.5 (86) (Fig. S20).

552 **Bayesian Parameter-Learning Procedure.** The λ values are optimized
 553 using a Bayesian parameter-learning procedure (30, 87, 88). The
 554 training set consists of the experimental R_g values of 42 IDPs
 555 (Tab. S1) and the intramolecular PRE data of six proteins (Tab. S2)
 556 (16, 22, 23, 37, 44–57). To guide the optimization within physically
 557 reasonable parameters and to avoid over-fitting the training set, we
 558 introduce a regularization term which penalizes deviations of the λ
 559 values from the probability distribution, $P(\lambda)$, which is the prior
 560 knowledge obtained from the statistical analysis of 87 hydrophobicity
 561 scales. The optimization procedure consists of the following steps
 562 (Fig. 2):

- 563 1. Single-chain CG simulation of the proteins of the training set
 564 (Tab. S1);
- 565 2. Conversion of CG simulations into all-atom trajectories using
 566 PULCHRA (89) of the proteins in Tab. S2 for the calculation
 567 of the PRE data;
- 568 3. Calculation of per-frame radii of gyration and PRE data. The
 569 PRE rates, Γ_2 , and intensity ratios, I_{para}/I_{dia} , are calculated

570 using the rotamer library approach implemented in DEER-
 571 PREdict (34) with $\tau_t = 100$ ps and optimizing the correlation
 572 time, $\tau_c \in [1, 10]$ ns, against the experimental data.

573 4. Random selection of six λ values which are nudged by random
 574 numbers picked from a normal distribution of standard devi-
 575 ation 0.05. The prior probability distribution, $P(\lambda)$, sets the
 576 bounds of the parameter space: any λ_i for which $P(\lambda_i) = 0$ is
 577 further nudged until $P(\lambda_i) \neq 0$.

578 5. Calculation of the Boltzmann weights for the i^{th} frame as
 579 $w_i = \exp[-[U(\mathbf{r}_i, \boldsymbol{\lambda}_k) - U(\mathbf{r}_i, \boldsymbol{\lambda}_0)]/k_B T]$, where $U(\mathbf{r}_i, \boldsymbol{\lambda}_k)$ and
 580 $U(\mathbf{r}_i, \boldsymbol{\lambda}_0)$ are the total Ashbaugh-Hatch energies of the i^{th}
 581 frame for trial and initial λ values, respectively. If the effective
 582 fraction of frames,

$$\phi_{eff} = \exp \left[- \sum_i^{N_{frames}} w_i \log (w_i \times N_{frames}) \right], \quad [1] \quad 583$$

584 is below 30%, the trial $\boldsymbol{\lambda}_k$ is discarded.

585 6. The per-frame radii of gyration and PRE observables are
 586 reweighted and the extent of agreement with the experimental
 587 data is estimated as

$$\chi_{R_g}^2 = \left(\frac{R_g^{exp} - R_g^{calc}}{\sigma_{R_g}^{exp}} \right)^2 \quad [2] \quad 588$$

589 and

$$\chi_{PRE}^2 = \frac{1}{N_{labels} N_{res}} \sum_j^{N_{labels}} \sum_i^{N_{res}} \left(\frac{Y_{ij}^{exp} - Y_{ij}^{calc}}{\sigma_{ij}^{exp}} \right)^2 \quad [3] \quad 590$$

591 where σ_{ij}^{exp} is the error on the experimental values, Y is either
 592 I_{para}/I_{dia} or Γ_2 , N_{labels} is the number of spin-labeled mutants
 593 and N_{res} is the number of measured residues;

594 7. Following the Metropolis criterion (90), the k^{th} set of λ values
 595 is accepted with probability:

$$A_{k-1 \rightarrow k} = \begin{cases} \exp \left[\frac{\mathcal{L}(\boldsymbol{\lambda}_{k-1}) - \mathcal{L}(\boldsymbol{\lambda}_k)}{\xi_k} \right], & \mathcal{L}(\boldsymbol{\lambda}_k) > \mathcal{L}(\boldsymbol{\lambda}_{k-1}) \\ 1, & \mathcal{L}(\boldsymbol{\lambda}_k) \leq \mathcal{L}(\boldsymbol{\lambda}_{k-1}), \end{cases} \quad [4] \quad 596$$

597 where the control parameter, ξ_k , scales with the number of
 598 iterations as $\xi = \xi_0 \times 0.99^k$. \mathcal{L} is the cost function

$$\mathcal{L}(\boldsymbol{\lambda}) = \langle \chi_{R_g}^2(\boldsymbol{\lambda}) \rangle + \eta \langle \chi_{PRE}^2(\boldsymbol{\lambda}) \rangle - \theta \sum_i \ln [P(\lambda_i)] \quad [5] \quad 599$$

600 where $\langle \chi_{R_g}^2(\boldsymbol{\lambda}) \rangle$ and $\langle \chi_{PRE}^2(\boldsymbol{\lambda}) \rangle$ are averages over the proteins
 601 in the training sets. θ and η are hyperparameters of the
 602 optimization procedure. θ determines the trade-off between
 603 between over- and under-fitting the training set whereas η sets
 604 the relative weight of the PRE data with respect to the radii
 605 of gyration.

606 Steps 4–7 are iterated until $\xi < 10^{-15}$, when the reweighting cycle
 607 is interrupted and new CG simulation carried out with the trained
 608 λ values. A complete parameter-learning procedure consists of two
 609 reweighting cycles starting from $\xi_0 = 2$ followed by three cycles
 610 starting from $\xi_0 = 0.1$. The threshold on ϕ_{eff} results in average
 611 absolute differences between χ^2 values estimated from reweighting
 612 and calculated from trajectories performed with the corresponding
 613 parameters of ~ 1.8 and ~ 0.8 for $\eta \chi_{PRE}^2$ and $\chi_{R_g}^2$, respectively
 614 (Fig. S24).

615 **Data deposition.** Datasets, code and Jupyter Notebooks for repro-
 616 ducing our analyses are available on GitHub at github.com/KULL-
 617 [Centre/papers/tree/main/2021/CG-IDPs-Tesei-et-al](https://github.com/KULL-Centre/papers/tree/main/2021/CG-IDPs-Tesei-et-al) and on Zen-
 618odo, DOI: [10.5281/zenodo.5005953](https://doi.org/10.5281/zenodo.5005953).

619 **ACKNOWLEDGMENTS.** We thank Veronica Ryan and Nicolas L.
 620 Fawzi for sharing the PRE data for FUS LCD, FUS12E LCD and A2
 621 LCD as well as Robert Konrat for sharing the intramolecular PRE
 622

622 data for Osteopontin. We thank Robert B. Best for sharing data
623 on compaction of IDPs, Gregory L. Dignon and Jeetain Mittal for
624 help setting up simulations with the HPS model, and Tanja Mittag,
625 Massimiliano Bonomi and Benjamin Schuler for helpful discussions.
626 We acknowledge funding from the BRAINSTRUC structural biology
627 initiative from the Lundbeck Foundation (R155-2015-2666), and
628 acknowledge access to computational resources from the ROBUST
629 Resource for Biomolecular Simulations (supported by the Novo
630 Nordisk Foundation; NNF18OC0032608) and Biocomputing Core
631 Facility at the Department of Biology, University of Copenhagen.
632 T.K.S. acknowledges support from the Novo Scholarship Programme
633 2021. This project has received funding from the European Union's
634 Horizon 2020 research and innovation programme under the Marie
635 Skłodowska-Curie grant agreement No. 101025063.

1. A Patel, et al., A liquid-to-solid phase transition of the ALS protein FUS accelerated by disease mutation. *Cell* **182**, 1066–1077 (2015).
2. S Wegmann, et al., Tau protein liquid–liquid phase separation can initiate tau aggregation. *The EMBO J.* **37**, e98049 (2018).
3. NM Kanaan, C Hamel, T Grabsinski, B Combs, Liquid–liquid phase separation induces pathogenic tau conformations in vitro. *Nat. Commun.* **11**, 2809 (2020).
4. S Ray, et al., α -synuclein aggregation nucleates through liquid–liquid phase separation. *Nat. Chem.* **12**, 705–716 (2020).
5. MC Hardenberg, et al., Observation of an α -synuclein liquid droplet state and its maturation into Lewy body-like assemblies. *J. Mol. Cell Biol.* **n/a** (2021) mjaia075.
6. Y Shin, CP Brangwynne, Liquid phase condensation in cell physiology and disease. *Science* **357**, eaaf4382 (2017).
7. NB Nedelsky, JP Taylor, Bridging biophysics and neurology: aberrant phase transitions in neurodegenerative disease. *Nat. Rev. Neuro.* **15**, 272–286 (2019).
8. TJ Nott, et al., Phase transition of a disordered nudge protein generates environmentally responsive membraneless organelles. *Mol. Cell* **57**, 936–947 (2015).
9. CP Brangwynne, P Tompa, RV Pappu, Polymer physics of intracellular phase transitions. *Nat. Phys.* **11**, 899–904 (2015).
10. RM Vernon, et al., Pi-pi contacts are an overlooked protein feature relevant to phase separation. *eLife* **7** (2018).
11. BS Schuster, et al., Identifying sequence perturbations to an intrinsically disordered protein that determine its phase-separation behavior. *Proc. Natl. Acad. Sci.* **117**, 11421–11431 (2020).
12. GL Dignon, RB Best, J Mittal, Biomolecular phase separation: From molecular driving forces to macroscopic properties. *Annu. Rev. Phys. Chem.* **71**, 53–75 (2020).
13. JP Brady, et al., Structural and hydrodynamic properties of an intrinsically disordered region of a germ cell-specific protein on phase separation. *Proc. Natl. Acad. Sci.* **114**, E8194–E8203 (2017).
14. J Wang, et al., A molecular grammar governing the driving forces for phase separation of prion-like RNA binding proteins. *Cell* **174**, 688–699.e16 (2018).
15. EW Martin, et al., Valence and patterning of aromatic residues determine the phase behavior of prion-like domains. *Science* **367**, 694–699 (2020).
16. A Bremer, et al., Deciphering how naturally occurring sequence features impact the phase behaviors of disordered prion-like domains. *bioRxiv* **n/a** (2021).
17. G Kainer, et al., Reentrant liquid condensate phase of proteins is stabilized by hydrophobic and non-ionic interactions. *Nat. Commun.* **12** (2021).
18. M Vazdar, et al., Arginine “magic”: Guanidinium-like-charge ion pairing from aqueous salts to cell penetrating peptides. *Accounts Chem. Res.* **51**, 1455–1464 (2018).
19. MJ Fossat, X Zeng, RV Pappu, Uncovering differences in hydration free energies and structures for model compound mimics of charged side chains of amino acids. *The J. Phys. Chem. B* **125**, 4148–4161 (2021).
20. GL Dignon, W Zheng, RB Best, YC Kim, J Mittal, Relation between single-molecule properties and phase behavior of intrinsically disordered proteins. *Proc. Natl. Acad. Sci.* **115**, 9929–9934 (2018).
21. GL Dignon, W Zheng, YC Kim, RB Best, J Mittal, Sequence determinants of protein phase behavior from a coarse-grained model. *PLOS Comput. Biol.* **14**, e1005941 (2018).
22. VH Ryan, et al., Mechanistic view of hnRNP A2 low-complexity domain structure, interactions, and phase separation altered by mutation and arginine methylation. *Mol. Cell* **69**, 465–479.e7 (2018).
23. Z Monahan, et al., Phosphorylation of the FUS low-complexity domain disrupts phase separation, aggregation, and toxicity. *The EMBO J.* **36**, 2951–2967 (2017).
24. VH Ryan, et al., Tyrosine phosphorylation regulates hnRNP A2 granule protein partitioning and reduces neurodegeneration. *The EMBO J.* **40** (2020).
25. S Das, YH Lin, RM Vernon, JD Forman-Kay, HS Chan, Comparative roles of charge, π , and hydrophobic interactions in sequence-dependent phase separation of intrinsically disordered proteins. *Proc. Natl. Acad. Sci.* **117**, 28795–28805 (2020).
26. JM Choi, AS Holehouse, RV Pappu, Physical principles underlying the complex biology of intracellular phase transitions. *Annu. Rev. Biophys.* **49**, 107–133 (2020).
27. LH Kapcha, PJ Rossky, A simple atomic-level hydrophobicity scale reveals protein interfacial structure. *J. Mol. Biol.* **426**, 484–498 (2014).
28. RM Regy, J Thompson, YC Kim, J Mittal, Improved coarse-grained model for studying sequence-dependent phase separation of disordered proteins. *Protein Sci.* **n/a** (2021).
29. DW Urry, et al., Hydrophobicity scale for proteins based on inverse temperature transitions. *Biopolymers* **32**, 1243–1250 (1992).
30. AB Norgaard, J Ferkinghoff-Borg, K Lindorff-Larsen, Experimental parameterization of an energy function for the simulation of unfolded proteins. *Biophys. J.* **94**, 182–192 (2008).
31. LP Wang, TJ Martinez, VS Pande, Building force fields: An automatic, systematic, and reproducible approach. *The J. Phys. Chem. Lett.* **5**, 1885–1891 (2014).
32. G Tiana, L Giorgetti, *Coarse Graining of a Giant Molecular System: The Chromatin Fiber*, eds. M Bonomi, C Camilloni. (Springer New York, New York, NY), pp. 399–411 (2019). 704
705
33. T Dannenhoffer-Lafage, RB Best, A data-driven hydrophobicity scale for predicting liquid–liquid phase separation of proteins. *The J. Phys. Chem. B* **125**, 4046–4056 (2021). 706
707
34. G Tesei, et al., DEER-PREdict: Software for efficient calculation of spin-labeling EPR and NMR data from conformational ensembles. *PLOS Comput. Biol.* **17**, e1008551 (2021). 708
709
35. KA Burke, AM Janke, CL Rhine, NL Fawzi, Residue-by-residue view of in vitro FUS granules that bind the C-terminal domain of RNA polymerase II. *Mol. Cell* **60**, 231–241 (2015). 710
711
36. AC Murthy, et al., Molecular interactions underlying liquid–liquid phase separation of the FUS low-complexity domain. *Nat. Struct. & Mol. Biol.* **26**, 637–648 (2019). 712
713
37. MM Dedmon, K Lindorff-Larsen, J Christodoulou, M Vendruscolo, CM Dobson, Mapping long-range interactions in α -synuclein using spin-label NMR and ensemble molecular dynamics simulations. *J. Am. Chem. Soc.* **127**, 476–477 (2005). 714
715
38. HS Chan, *Amino Acid Side-chain Hydrophobicity*. (American Cancer Society), (2002). 716
717
39. S Simm, J Einloft, O Mirus, E Schleif, 50 years of amino acid hydrophobicity scales: revisiting the capacity for peptide classification. *Biol. Res.* **49** (2016). 718
719
40. HB Bull, K Breese, Surface tension of amino acid solutions: A hydrophobicity scale of the amino acid residues. *Arch. Biochem. Biophys.* **161**, 665–670 (1974). 720
721
41. H Guy, Amino acid side-chain partition energies and distribution of residues in soluble proteins. *Biophys. J.* **47**, 61–70 (1985). 722
723
42. CM Bishop, WF Walkenhorst, WC Wimley, Folding of β -sheets in membranes: specificity and promiscuity in peptide model systems. *J. Mol. Biol.* **309**, 975–988 (2001). 724
725
43. GW Welling, WJ Weijer, R van der Zee, S Welling-Westerveld, Prediction of sequential antigenic regions in proteins. *FEBS Lett.* **188**, 215–218 (1985). 726
727
44. S Jephthah, L Staby, BB Kragelund, M Skepö, Temperature dependence of intrinsically disordered proteins in simulations: What are we missing? *J. Chem. Theory Comput.* **15**, 2672–2683 (2019). 728
729
45. E Fagerberg, LK Måansson, S Lenton, M Skepö, The effects of chain length on the structural properties of intrinsically disordered proteins in concentrated solutions. *The J. Phys. Chem. B* **124**, 11843–11853 (2020). 730
731
46. M Kjaergaard, et al., Temperature-dependent structural changes in intrinsically disordered proteins: Formation of α -helices or loss of polyproline II? *Protein Sci.* **19**, 1555–1564 (2010). 732
733
47. GNW Gomes, et al., Conformational ensembles of an intrinsically disordered protein consistent with NMR, SAXS, and single-molecule FRET. *J. Am. Chem. Soc.* **142**, 15697–15710 (2020). 734
735
48. UR Shrestha, et al., Generation of the configurational ensemble of an intrinsically disordered protein from unbiased molecular dynamics simulation. *Proc. Natl. Acad. Sci.* **116**, 20446–20452 (2019). 736
737
49. CL Johnson, et al., The two-state prehensile tail of the antibacterial toxin colicin n. *Biophys. J.* **113**, 1673–1684 (2017). 738
739
50. AD Biasio, et al., p15paf is an intrinsically disordered protein with nonrandom structural preferences at sites of interaction with other proteins. *Biophys. J.* **106**, 865–874 (2014). 740
741
51. A Paz, et al., Biophysical characterization of the unstructured cytoplasmic domain of the human neuronal adhesion protein neuroligin 3. *Biophys. J.* **95**, 1928–1944 (2008). 742
743
52. JA Riback, et al., Innovative scattering analysis shows that hydrophobic disordered proteins are expanded in water. *Science* **358**, 238–241 (2017). 744
745
53. MC Ahmed, et al., Refinement of α -synuclein ensembles against SAXS data: Comparison of force fields and methods. *Front. Mol. Biosci.* **8** (2021). 746
747
54. E Mylonas, et al., Domain conformation of tau protein studied by solution small-angle x-ray scattering. *Biochemistry* **47**, 10345–10353 (2008). 748
749
55. G Platzter, et al., The metastasis-associated extracellular matrix protein osteopontin forms transient structure in ligand interaction sites. *Biochemistry* **50**, 6113–6124 (2011). 750
751
56. T Mittag, et al., Structure/function implications in a dynamic complex of the intrinsically disordered sic1 with the cdc4 subunit of an SCF ubiquitin ligase. *Structure* **18**, 494–506 (2010). 752
753
57. D Kurzbach, et al., Detection of correlated conformational fluctuations in intrinsically disordered proteins through paramagnetic relaxation interference. *Phys. Chem. Chem. Phys.* **18**, 5753–5758 (2016). 754
755
58. AZ Panagiotopoulos, V Wong, MA Floriano, Phase equilibria of lattice polymers from histogram reweighting monte carlo simulations. *Macromolecules* **31**, 912–918 (1998). 756
757
59. YH Lin, HS Chan, Phase separation and single-chain compactness of charged disordered proteins are strongly correlated. *Biophys. J.* **112**, 2043–2046 (2017). 758
759
60. UR Shrestha, JC Smith, L Petridis, Full structural ensembles of intrinsically disordered proteins from unbiased molecular dynamics simulations. *Commun. Biol.* **4** (2021). 760
761
61. JA Greig, et al., Arginine-enriched mixed-charge domains provide cohesion for nuclear speckle condensation. *Mol. Cell* **77**, 1237–1250 (2020). 762
763
62. RS Fisher, S Elbaum-Garfinkle, Tunable multiphase dynamics of arginine and lysine liquid condensates. *Nat. communications* **11**, 1–10 (2020). 764
765
63. WC Wimley, SH White, Experimentally determined hydrophobicity scale for proteins at membrane interfaces. *Nat. Struct. & Mol. Biol.* **3**, 842–848 (1996). 766
767
64. P Ponnuswamy, MM Gromiha, Prediction of transmembrane helices from hydrophobic characteristics of proteins. *Int. J. Pept. Protein Res.* **42**, 326–341 (2009). 768
769
65. MD Mukrasch, et al., Structural polymorphism of 441-residue tau at single residue resolution. *PLoS Biol.* **7**, e1000034 (2009). 770
771
66. AJ Lopez, PK Quioka, M Linke, G Hummer, J Kofinger, Quantifying protein–protein interactions in molecular simulations. *The J. Phys. Chem. B* **124**, 4673–4685 (2020). 772
773
67. S Elbaum-Garfinkle, et al., The disordered p granule protein LAF-1 drives phase separation into droplets with tunable viscosity and dynamics. *Proc. Natl. Acad. Sci.* **112**, 7189–7194 (2015). 774
775
68. MT Wei, et al., Phase behaviour of disordered proteins underlying low density and high permeability of liquid organelles. *Nat. Chem.* **9**, 1118–1125 (2017). 776
777
69. NO Taylor, MT Wei, HA Stone, CP Brangwynne, Quantifying dynamics in phase-separated condensates using fluorescence recovery after photobleaching. *Biophys. J.* **117**, 1285–1300 (2019). 778
779
70. GL Dignon, W Zheng, YC Kim, J Mittal, Temperature-controlled liquid–liquid phase separation 780
781

788 of disordered proteins. *ACS Cent. Sci.* **5**, 821–830 (2019).

789 71. TT Foley, MS Shell, WG Noid, The impact of resolution upon entropy and information in
790 coarse-grained models. *The J. Chem. Phys.* **143**, 243104 (2015).

791 72. J Jin, AJ Pak, GA Voth, Understanding missing entropy in coarse-grained systems: Address-
792 ing issues of representability and transferability. *The J. Phys. Chem. Lett.* **10**, 4549–4557
793 (2019).

794 73. G Tesei, et al., Self-association of a highly charged arginine-rich cell-penetrating peptide.
795 *Proc. Natl. Acad. Sci.* **114**, 11428–11433 (2017).

796 74. X Zeng, AS Holehouse, A Chilkoti, T Mittag, RV Pappu, Connecting coil-to-globule transitions
797 to full phase diagrams for intrinsically disordered proteins. *Biophys. J.* **119**, 402–418 (2020).

798 75. J Wimr, W Peti, H Schwalbe, Motional properties of unfolded ubiquitin: a model for a ran-
799 dom coil protein. *J. biomolecular NMR* **35**, 175–186 (2006).

800 76. G Raos, G Allegra, Chain collapse and phase separation in poor-solvent polymer solutions:
801 A unified molecular description. *The J. chemical physics* **104**, 1626–1645 (1996).

802 77. J Wen, et al., Conformational expansion of tau in condensates promotes irreversible aggre-
803 gation. *J. Am. Chem. Soc.* **143**, 13056–13064 (2021).

804 78. AP Latham, B Zhang, Maximum entropy optimized force field for intrinsically disordered pro-
805 teins. *J. chemical theory computation* **16**, 773–781 (2019).

806 79. S Elbaum-Garfinkle, Matter over mind: Liquid phase separation and neurodegeneration. *J.*
807 *Biol. Chem.* **294**, 7160–7168 (2019).

808 80. DG Brown, J Shorter, HJ Wobst, Emerging small-molecule therapeutic approaches for amy-
809 otrophic lateral sclerosis and frontotemporal dementia. *Bioorganic & Medicinal Chem. Lett.*
810 **30**, 126942 (2020).

811 81. A Siegert, et al., Interplay between tau and α -synuclein liquid–liquid phase separation. *Pro-
tein Sci.* **n/a** (2021).

812 82. KM Ruff, F Dar, RV Pappu, Polyphasic linkage and the impact of ligand binding on the regu-
813 lation of biomolecular condensates. *Biophys. Rev.* **2**, 021302 (2021).

814 83. TM Perdikari, et al., A predictive coarse-grained model for position-specific effects of post-
815 translational modifications. *Biophys. J.* **120**, 1187–1197 (2021).

816 84. S Wohl, M Jakubowski, W Zheng, Salt-dependent conformational changes of intrinsically
817 disordered proteins. *The J. Phys. Chem. Lett.* **12**, 6684–6691 (2021).

818 85. JA Anderson, J Glaser, SC Glotzer, HOOMD-blue: A python package for high-performance
819 molecular dynamics and hard particle monte carlo simulations. *Comput. Mater. Sci.* **173**,
820 109363 (2020).

821 86. P Eastman, et al., OpenMM 7: Rapid development of high performance algorithms for molec-
822 ular dynamics. *PLOS Comput. Biol.* **13**, e1005659 (2017).

823 87. A Cesari, et al., Fitting corrections to an rna force field using experimental data. *J. chemical
824 theory computation* **15**, 3425–3431 (2019).

825 88. S Orioli, AH Larsen, S Bottaro, K Lindorff-Larsen, How to learn from inconsistencies: Inte-
826 grating molecular simulations with experimental data in *Computational Approaches for Un-
827 derstanding Dynamical Systems: Protein Folding and Assembly*. (Elsevier), pp. 123–176
828 (2020).

829 89. P Rotkiewicz, J Skolnick, Fast procedure for reconstruction of full-atom protein models from
830 reduced representations. *J. Comput. Chem.* **29**, 1460–1465 (2008).

831 90. PC Schuur, Classification of acceptance criteria for the simulated annealing algorithm. *Math.
832 Oper. Res.* **22**, 266–275 (1997).

833